Showcasing research from Roy Goodacre's laboratory, Department of Biochemistry, Institute of Integrative Biology, University of Liverpool, UK.

Rapid differentiation of *Campylobacter jejuni* cell wall mutants using Raman spectroscopy, SERS and mass spectrometry combined with chemometrics

Analytical methods for bacterial characterisation usually measure the whole organism. We consider the location of the measurement within and on bacteria to be important. To investigate this a major cause of foodborne gastroenteritis worldwide was studied with *C. jejuni* mutants which have been designed to disrupt the production of prominent surface features of the bacterium: including capsule, flagella and glycoproteins. We compare and contrast cell wall *versus* cytoplasma SERS approaches with Raman and MALDI-MS and show these are capable of identifying cell wall mutants of a single isogenic bacterial strain.

ROYAL SOCIETY
OF **CHEMISTRY**

rsc.li/analyst

Rapid differentiation of *Campylobacter jejuni* cell wall mutants using Raman spectroscopy, SERS and mass spectrometry combined with chemometrics†

Malama Chisanga,[a] Dennis Linton,[b] Howbeer Muhamadali,[c] David I. Ellis, [ID][a] Richard L. Kimber, [ID][d] Aleksandr Mironov [ID][e] and Royston Goodacre [ID] *[c]

The Gram-negative bacterial pathogen *Campylobacter jejuni* is a major cause of foodborne gastroenteritis worldwide. Rapid detection and identification of *C. jejuni* informs timely prescription of appropriate therapeutics and epidemiological investigations. Here, for the first time, we report the applicability of Raman spectroscopy, surface-enhanced Raman scattering (SERS) and matrix-assisted laser desorption/ionisation mass spectrometry (MALDI-TOF-MS) combined with chemometrics, for rapid differentiation and characterisation of mutants of a single isogenic *C. jejuni* strain that disrupt the production of prominent surface features (capsule, flagella and glycoproteins) of the bacterium. Multivariate analysis of the spectral data obtained from these different physicochemical tools revealed distinctive biochemical differences which consistently discriminated between these mutants. In order to generate biochemical and phenotypic information from different locations in the cell—cell wall *versus* cytoplasm — we developed two different *in situ* methods for silver nanoparticle (AgNP) production, and compared this with *simple mixing* of bacteria with pre-synthesised AgNPs. This SERS trilogy (*simple mixing* with premade AgNPs and two *in situ* AgNP production methods) presents an integrated platform with potential for rapid, accurate and confirmatory detection of pathogenic bacteria based on cell envelope or intracellular molecular dynamics. Our spectral findings demonstrate that Raman, SERS and MALDI-TOF-MS are powerful metabolic fingerprinting techniques capable of discriminating clinically relevant cell wall mutants of a single isogenic bacterial strain.

Introduction

Foodborne bacterial diseases are a global health challenge associated with high morbidity and mortality.[1] Common bacterial pathogens which are responsible for foodborne infections include *Escherichia coli* O157, *Listeria monocytogenes*, *Campylobacter* and *Salmonella* spp.[2] Human campylobacteriosis is considered the leading form of food poisoning worldwide.[1,3] Several foodborne infection cases predominantly implicate *C. jejuni* strains as the leading etiological agents of campylobacteriosis.[4,5] Recently, a survey of foodborne infections in the European Union reported a notification rate of 64.8 per 100 000 population for *C. jejuni* infections,[6] which has increased substantially within the recent decade.[3] Although specific outbreaks of *Campylobacter* food poisoning are uncommon, the many apparently sporadic cases are a significant public health problem causing a substantial global economic burden.[4]

Numerous epidemiological studies have identified contaminated chicken as the major source of *Campylobacter* infection,[1,6] although other poultry are also reservoirs.[7] The widespread consumption of chicken, a relatively inexpensive protein source, undoubtedly contributes to the scale of human *C. jejuni* infections. Whilst *C. jejuni* infection typically results in self-limiting gastroenteritis in humans, it can also lead to more serious outcomes such as reactive arthritis and Guillain-Barré syndrome involving acute neuromuscular paralysis.[8,9] Thus, rapid detection of *C. jejuni* in real time is important for quick and effective surveillance, remediation and timely prescription of appropriate medication.

During infection, *C. jejuni* colonises the mucus layer in the gut and can also invade epithelial cells. Important virulence factors include the capsular polysaccharide (CPS), bipolar

[a] School of Chemistry, Manchester Institute of Biotechnology, University of Manchester, Manchester, M1 7DN, UK
[b] School of Biological Sciences, Faculty of Biology, Medicine and Health, University of Manchester, Manchester, M13 9PL, UK
[c] Department of Biochemistry, Institute of Integrative Biology, University of Liverpool, Liverpool, L69 7ZB, UK. E-mail: roy.goodacre@liverpool.ac.uk;
Tel: +44 (0)151 795 7689
[d] Department of Earth and Environmental Sciences, University of Manchester, Manchester, M13 9PL, UK
[e] EM Core Facility, Faculty of Biology, Medicine and Health, University of Manchester, Manchester, M13 9PL, UK
†Electronic supplementary information (ESI) available. See DOI: 10.1039/c9an02026h

flagella that mediate cell motility, and the *N*-linked general protein glycosylation system that modifies a large number of surface located proteins.[9,10] Accurate characterisation of *C. jejuni* based on biochemical dynamics and associated phenotypes may improve our understanding of the pathogenesis of campylobacteriosis and how *C. jejuni* interact with the human gut.[11]

Culture, along with morphological and biochemical tests, are the gold standard tools for the detection, isolation and identification of pathogens in healthcare systems, though alternative analytical techniques have been proposed.[12] However, traditional microbiological methods are time consuming, and biochemical tests are prone to false negative results,[12,13] since they do not detect biochemically unreactive clinical isolates.[14] Although real-time polymerase chain reaction (PCR) can overcome these limitations by providing more sensitive and reliable taxonomy of microbes rapidly,[15] it does not characterise real bacterial phenotypes and cannot differentiate between viable and non-viable microbes.[12,16]

Recently, Raman spectroscopy has emerged as an alternative molecularly specific tool for rapid, accurate, non-destructive and label-free characterisation of pathogens down to the strain level.[17] A Raman spectrum can be described as a typical whole-organism biochemical fingerprint derived from intact bacterial cells, consisting of vibrational modes from molecules including metabolites, nucleic acids, proteins, lipids and carbohydrates.[18] Consequently, Raman spectra can be utilised to infer strain-specific physiological, metabolic and phenotypic states of bacterial cells.[19,20] However, Raman spectroscopy has limited sensitivity owing to its inherently poor quantum efficiency.[21] Surface-enhanced Raman scattering (SERS) can be used to amplify Raman signals up to several orders of magnitude when a sample is in the close vicinity or adsorbed onto plasmonic materials such as metallic nanoparticles (NP).[22] In addition to improving the sensitivity, SERS allows for selective deposition of NPs onto the bacterial cell wall or inside the cells.[23] Thus, when Raman and SERS are applied together, they potentially provide complementary biomolecular information capable of differentiating bacterial classes as well as inferring functional capability. That is to say, whilst Raman spectroscopy provides whole-bacterium biochemical information and phenotype, SERS may selectively unravel and amplify structural moieties and bond linkages located specifically on bacterial cell surface including lipopolysaccharides (LPS) and peptidoglycan, or intracellular biomolecules such as amino acids, carbohydrates and nucleobases.[24]

Matrix-assisted laser desorption/ionisation time-of-flight mass spectrometry (MALDI-TOF-MS) has also gained significant attention for routine phenotyping of clinical isolates such as *C. jejuni*,[25–27] *Bacillus*[28,29] and *Enterococcus*[30,31] spp. Interestingly, in recent years, MALDI-TOF-MS has been applied in parallel with Raman and SERS fingerprints for comprehensive biochemical characterisation of bacteria.[30] Similar to vibrational spectroscopy, MALDI-TOF-MS is rapid, robust and cost-effective, and elucidates structural dynamics specifically in physiologically essential cellular proteins, peptides and lipids biomarkers.[32] However, to achieve clinically desirable reproducibility for bacterial detection, MALDI-TOF-MS also requires carefully optimised procedures including the identification of appropriate matrix preparation and deposition methods for bacterial samples.[33]

In this study, we applied Raman spectroscopy, SERS and MALDI-TOF-MS for rapid and accurate differentiation of a panel of mutants within the otherwise isogenic *C. jejuni* strain that disrupted the production of key surface biochemical features (CPS, flagella and *N*-glycosylated proteins). For the first time, we employed label-free SERS involving *simple mixing* and *in situ* synthesis of AgNPs to probe molecular dynamics of pathogenic bacteria to complement Raman and MALDI-TOF-MS fingerprints with the help of chemometrics.

Experimental methods

Bacterial strains and cultivation conditions

The *C. jejuni* NCTC 11168H strain and derived mutants (for details see Table 1) were grown on Columbia agar (Oxoid) plates containing 5% horse blood (TCS Biosciences), obtained from a single batch. Inoculated agar plates were incubated in a MACS Variable Atmosphere Incubator (Don Whitley Scientific Ltd) containing a gas mixture of 85% N_2, 10% CO_2 and 5% O_2.

Sample preparation

Biomass for *C. jejuni* NCTC 11168H and derived mutants was harvested from the surface of agar plates after 24 h of incubation. Following harvesting using sterile inoculating loops, biomass was resuspended in physiological saline (0.9% NaCl) in Falcon tubes (Greiner Bio-One, Germany) and stored on ice throughout the sample preparation steps. Each bacterial strain or mutant was grown on four separate agar plates and these

Table 1 List of *C. jejuni* strain and derivative mutants investigated in this study, including descriptions and sources

Strain	Description	Mutations	Source/reference
11168H	Wild type	None	National collection of type cultures, U.K. Karlyshev *et al.*[99]
11168H *pglB*−	Cj1126::kn	Surface proteins lack heptasaccharide *N*-linked glycans	Linton laboratory
11168H *kpsM*−	Cj1448c::kn	Disrupted cytoplasmic CPS biosynthesis	Karlyshev *et al.*[42]
11168H *kpsS*−	Cj1413c::kn	Disrupted cytoplasmic CPS biosynthesis	Karlyshev *et al.*[42]
11168H *kpsC*−	Cj1414c::kn	Disrupted CPS transport to cell surface	Karlyshev *et al.*[42]
11168H *flaA*−	Cj1339c::kn	Lacks flagella	Linton laboratory

were used as biological replicates per sample ($n = 4$). Bacterial cell samples were washed twice in 0.9% NaCl by centrifugation at 4000g for 5 min at 4 °C using a bench top Eppendorf Centrifuge 5810 R (Hamburg, Germany), and resuspended in 2 mL of 0.9% NaCl. Optical densities of all cell suspensions were measured spectrophotometrically at 600 nm using an Eppendorf BioSpectrometer (Eppendorf, Cambridge, UK) and used to normalise biomass. All bacterial samples with normalised final OD$_{600}$ were stored at −80 °C prior to spectral analysis.

Transmission Electron Microscopy

The samples were fixed with 4% formaldehyde and 2.5% glutaraldehyde in 0.1 M HEPES buffer (pH 7.2). Then they were post-fixed with 1% osmium tetroxide and 1.5% potassium ferrocynaide in 0.1 M cacodylate buffer (pH 7.2) for 1 h and in 1% uranyl acetate in water for 1 h. The samples were dehydrated in an ethanol series infiltrated with TAAB 812 resin and polymerized for 24 h at 60 °C. Finally, 70 nm sections were cut with Reichert Ultracut ultramicrotome and observed with a FEI Tecnai 12 Biotwin microscope at 80 kV accelerating voltage. Images were taken with a Gatan Orius SC1000 CCD camera.

Synthesis of colloidal silver NPs (AgNPs)

All glassware was washed with aqua regia (1 part of HNO$_3$ and 3 parts of HCl), rinsed in deionised water and dried in a fume hood prior to AgNPs synthesis.

The synthetic routes for *in situ* methods followed our previously reported protocols,[34] similar to those described in detail by Efrima and Zeiri.[23] For the *in situ* SERS method involving deposition of AgNPs around cell walls (*in situ* external), cell pellets were suspended in ice-cold 0.09 M NaBH$_4$ solution acting as a reductant, followed by 5 min centrifugation at 2800g at 4 °C. After discarding supernatants, each pellet was resuspended in ice-cold 0.04 M AgNO$_3$ solution. At this point, a redox reaction occurred resulting in the production of AgNPs on the cell wall as demonstrated recently.[34] To effect the *in situ* protocol for deposition of AgNPs inside cells (*in situ* internal), ice-cold reductant and oxidant were added in reverse order; that is to say, the pelleted biomass initially suspended in 0.04 M AgNO$_3$ solution and centrifuged for 5 min at 2800g at 4 °C, were re-dissolved in 0.09 M NaBH$_4$ solution.

In the *simple mixing* SERS, AgNPs were synthesised prior to mixing with cell suspensions. The method described by Creighton,[35] was modified as follows: aqueous solutions of 0.09 M NaBH$_4$ and 0.04 M AgNO$_3$ were separately prepared and kept on an ice-bath for 1 h. Ice-cold AgNO$_3$ solution was slowly added dropwise to ice-cold NaBH$_4$ with vigorous stirring in the fume hood. The reaction mixture changed colour from clear solution to milky yellow and finally dark green, confirming successful AgNP production. The resulting solution was left stirring for 15 min to stabilise colloidal NP sizes. The flasks containing colloidal suspensions were wrapped in aluminium foils and stored in the dark prior to SERS analysis. Using UV/Vis spectrophotometry, the absorption maximum for borohydride-reduced AgNPs was detected at 390 nm. These

pre-formed AgNPs were mixed with bacterial cell suspension in an optimal volume (μL) ratio of 20 : 1 that resulted in the best SERS signal enhancement.

Raman and SERS spectroscopic analysis

Prior to Raman and SERS measurements, 2 μL sample aliquots were spotted, in a random order, on to clean CaF$_2$ discs and dried for 30 min at room temperature. Spectral analysis was performed in confocal mode on an InVia confocal Raman spectrometer (Renishaw Plc., Gloucestershire, UK) equipped with a 785 nm near infrared diode laser and 600 lines per mm grating, giving a spectral resolution of 6 cm^{-1} as we reported previously.[36] The Raman instrument was calibrated with the phonon band of a Si wafer visualised under a 50× objective (NA = 0.9) and collected as a static spectrum centered at 520 cm^{-1}. For Raman spectroscopy, the laser power was adjusted to 30 mW on the sample with an exposure time of 15 s and 4 spectral accumulations. SERS analysis was carried out by irradiating laser power of 0.3 mW onto dried bacteria-AgNPs samples for 2 s with single spectral accumulation. To account for biological and spectral variations, three spectra were acquired from different positions of each sample spot chosen manually.

MALDI-TOF-MS analysis

Sample preparation for MALDI-TOF-MS followed the protocol reported by AlMasoud and co-workers.[30] The matrix was prepared by dissolving 10 mg of sinapinic acid in 500 μL of 2% trifluoroacetic acid (TFA) and 500 μL acetonitrile aqueous solutions. Cell pellets were resuspended in 0.1% TFA aqueous solution and mixed with an equal volume (10 μL) of the matrix and vortexed for 2 s to obtain homogenous solutions. For each matrix-bacteria mixture, 2 μL was immediately spotted on to a MALDI stainless steel plate and air-dried for 1 h before spectral acquisition.

An AXIMA-Confidence MALDI-TOF mass spectrometer (Shimadzu Biotech, Manchester, UK) equipped with a nitrogen pulsed UV laser with 337 nm wavelength was used for data acquisition. The instrument was calibrated with a homogenous mixture of proteins, *viz.* insulin (5735 Da), cytochrome *c* (12 362 Da) and apomyoglobin (16 952 Da),[25] prior to spectral data measurements from dried bacterial-matrix samples. A total of 100 profiles, each containing 20 shots, were collected using a circular raster pattern and the laser head power set to 120 mV. The MALDI-TOF-MS instrument was operated in the positive ionisation mode (EI) and linear TOF set up, and mass spectra were acquired between 400–12 000 mass-to-charge ratios (m/z). Spectral collection time was ~3 min per sample.

Data processing and analysis

MATLAB software version 2017a (The MathWorks Inc., Natwick, US) was used for all multivariate statistical analyses. A typical procedure for pre-processing of spectral data was conducted as follows. All acquired Raman, SERS and MALDI-TOF-MS data were separately baseline corrected using

the asymmetric least squares (AsLS) algorithm.[37] Raman and SERS spectra were scaled using the extended multiplicative signal correction (EMSC),[38] whilst mass spectra were $\log_{10}$ scaled prior to multivariate cluster analysis.

The unsupervised modelling of principal component analysis (PCA) was employed to reduce the dimensionality of data, and explore natural differences and similarities between bacteria using Raman and SERS data.[39] However, due to the complexity of MALDI-TOF-MS data (101 000 data points × 6 samples × 3 replicates), discriminant function analysis (DFA) was used to discriminate between *C. jejuni* strain and mutants on the basis of 30 retained principal components (PCs) and *a priori* knowledge from spectral replicates and strain metadata. DFA minimises within-class and simultaneously maximising between-class variance in a dataset.[40] To simplify the interpretation of scores plots, hierarchical cluster analysis (HCA),[41] based on mean scores for PCA (Raman and SERS) and DFA (MALDI-TOF-MS) using the Ward's linkage, were generated to visualise the relatedness of mutants through dendrograms.

Results

Understanding biochemical composition and structural dynamics in pathogens is undoubtedly essential for elucidating roles of biomolecules in the development of human gastroenteritis and for probing molecular targets to guide therapeutic development. In this study, we applied Raman spectroscopy, SERS and MALDI-TOF-MS platforms to differentiate and characterise structurally diverse bacterial mutants derived from a single *C. jejuni* wild type strain based on chemical capabilities and phenotypes. Amongst the investigated bacteria, the $kpsC^-$, $kpsS^-$ and $kpsM^-$ mutants exhibited closely related phenotypes, which are mediated by the changes in CPS. The CPS is an essential and structurally unique extracellular biomolecule, which is the major determinant of *C. jejuni* serotype.[10] The KpsC, KpsS and KpsM proteins are involved in the production and transportation of CPS to *C. jejuni* cell surface.[42] Another vital extracellular virulence factor is the flagellum,[43] which enables cell locomotion. The flagellum consists of a basal body, hook and long filament protruding from the cell surface. The flagellar filament contains several proteins, including FlaA, which facilitates the invasion of epithelial cells and plays a key role in the activation of host immune response.[44] Unlike other mutants tested in this study, the $flaA^-$ does not have flagellar filaments, due to lack of FlaA protein. In contrast, $plgB^-$ expresses unique phenotype driven by the absence of heptasaccharide *N*-linked glycans in surface proteins. All bacterial mutations are clearly depicted in Fig. 1.

Fig. 2 shows transmission electron microscope (TEM) images of thin sections of *C. jejuni* and spectra for AgNPs. Clearly AgNPs were located on the cell envelope when the *in situ* production method for external AgNPs and *simple mixing* SERS methods were applied (Fig. 2a and b). By contrast,
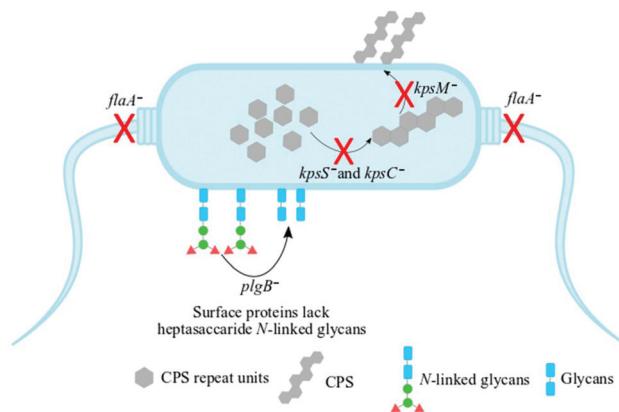
Fig. 1 A schematic representation of the mutants of *C. jejuni* 11168H strain examined in this study. The $kpsS^-$ and $kpsC^-$ mutants have disrupted cytoplasmic CPS biosynthesis while $kpsM^-$ is capable of biosynthesising cytoplasmic CPS but lacks the transport machinery of cytoplasmic CPS to the cell surface. The $flaA^-$ mutant lacks the flagellar filament whilst the $plgB^-$ strain contains numerous surface proteins which lack heptasaccharide *N*-linked glycans. Black arrows and red crosses indicate processes disrupted by the indicated mutations.

when AgNPs were synthesised *in situ* and located internally, the AgNPs were generated by silver ion reduction inside cells to produce Ag(0).

Raman fingerprints

Fig. 3a shows typical information-rich Raman spectral features arising from predominant biochemical components which were used to discriminate bacterial samples. Each Raman spectrum represents a mean of at least 8 spectra recorded from bacterial slurries examined in this study. The prominent Raman band at 1004 cm^{-1} is assigned to the ring breathing modes of phenylalanine.[16] The Raman band at 1340 cm^{-1} was also observed which is attributed to adenine ring vibrations displayed peak splitting pattern.[21] The amide I (C=O, C–N stretching and N–H bending) and amide III (C–N stretching and N–H bending) also showed intense peaks at 1661 and 1250 cm^{-1}, respectively.[45] Other bands of low intensity but diagnostically useful were recorded at 1575 cm^{-1} (ring breathing in guanine and adenine), 1143 cm^{-1} (C–N and C–C stretching in proteins), 1090 and 540 cm^{-1} (C–C skeletal and C–O–C stretching modes in glycosidic linkages in polysaccharides) and 783 cm^{-1} (ring breathing in DNA/RNA) and 965 cm^{-1} (lipids and polysaccharide modes).[45,46]

Fig. 4a illustrates PCA scores for *C. jejuni* NCTC 11168H strain and five derived (near isogenic) mutants (Table 1). Coloured clusters represent individual strain classes listed in Table 1. According to PC1 and PC2, all the strains clustered separately and away from each other; moreover, replicate samples clustered together illustrating excellent reproducibility. Notably, the $flaA^-$ mutant was clearly discriminated from the parental wild type *C. jejuni* (*C.j-WT*) and other derived mutants along PC1 (Fig. 4a). On the other hand, the *C.j-WT* and $pglB^-$ were clearly separated from other mutants according
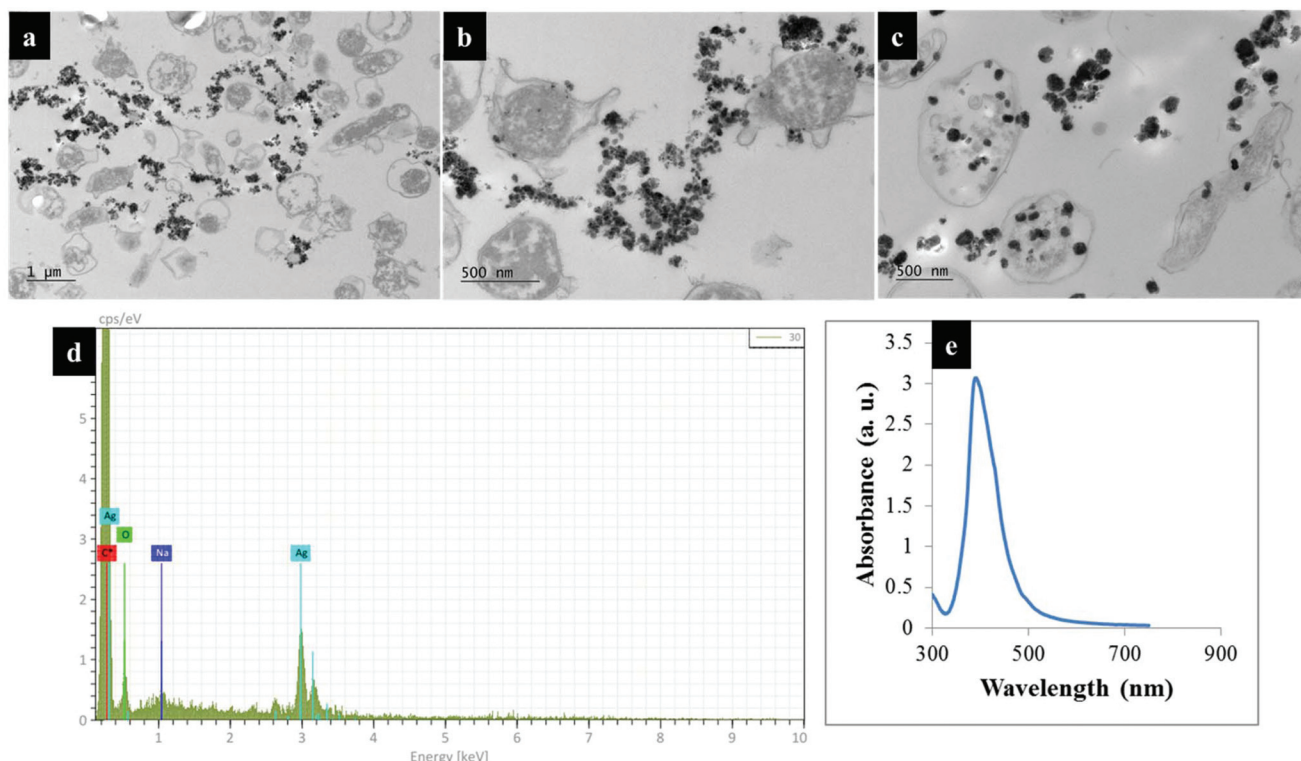
Fig. 2 TEM images of thin section of *C. jejuni* cells and AgNPs prepared *via* (a) *in situ* external, (b) *simple mixing* and (c) *in situ* internal SERS protocols; (d) the energy-dispersive X-ray (EDX) spectrum of bacteria-AgNPs indicating the presence of AgNPs in the sample mixtures and (e) UV/Vis plasmon spectrum for pre-formed AgNPs employed for the *simple mixing* protocols. Bacteria-AgNPs were diluted to reduce the density of NPs and bacterial cells. Thin sections of bacteria were used for TEM imaging to assist with clearer visualisation of AgNPs on bacterial cells.

to PC2. These observations were consistent with HCA dendrograms in Fig. 5a.

Interestingly, the $kpsM^-$, $kpsS^-$ and $kpsC^-$ mutants clustered close to each other and clearly separated away from the rest of the bacterial strains along PC1. The clusters for $kpsS^-$ and $kpsC^-$ are closer to each other and more distant from the $kpsM^-$. This discrimination between these three mutants was explored further by plotting PCA scores (Fig. 6). As shown on Fig. 6a, PC1 clearly separated $kpsM^-$ from $kpsS^-$ and $kpsC^-$ whilst PC2 differentiated between $kpsS^-$ and $kpsC^-$. According to the PC1 and PC2 loadings (Fig. S1†), the dominant variable associated with the separation patterns for these three mutants were a redshift (the peak shifted to a lower frequency) for symmetric ring breathing in phenylalanine (1006 to 999 cm^{-1}), adenine (1331 cm^{-1}), polysaccharides (1020–1065 cm^{-1}) and lipids (1461 cm^{-1}). A spectral band detected at 1091 cm^{-1}, which is assigned to C–C skeletal and C–O–C stretching for 1,4-glycosidic linkages in polysaccharides,[47] was more intense for $kpsM^-$ than the other *kps* mutants according to PC1 loadings (Fig. S1a†).

Next, the PC loadings plots (Fig. S2†) for Raman data of all the strains examined in this study were constructed to assess the significant variants associated with the clustering trends in the PCA scores plot (Fig. 4a). Examination of PC1 loadings (Fig. S2a†) revealed mainly intensity differences in phenylalanine (1004 cm^{-1}), alkyl CH$_2$ deformations in lipids and pro-

teins (1450 cm^{-1}), and C–C and C–O–C stretching mode of 1,4-glycosidic linkage (1209, 1099 and 856 cm^{-1}) vibrations,[21,45] which were higher for *C.j-WT*, $pglB^-$ and $flaA^-$. Other vibrations: C–N and C–C stretching in proteins (1143 cm^{-1}), adenine (1338 cm^{-1}), and adenine and guanine (1575 cm^{-1}) ring modes contributed significantly to strain differentiation on PC1. In addition to PC1 variables, PC2 loadings identified a redshift in phenylalanine ring symmetric breathing (1004–998 cm^{-1}) and COO$^-$ stretching in proteins (1400 cm^{-1}) as other explanatory inputs linked to PCA scores distribution in Fig. 4a.

SERS fingerprints

***In situ* production where nanoparticles are externally located.** For *in situ* external SERS, AgNPs formed layers around bacterial cells as shown in Fig. 2a. Fig. 3b shows SERS spectra for the *in situ* external mode which is typically characterised by sharp bands at 661, 730, 1055 and 1330 cm^{-1} that are usually weak in Raman spectra (Fig. 3a). PCA scores (Fig. 4b) demonstrate similar clustering patterns as the Raman data (Fig. 4a), revealing complete separation of $flaA^-$ from the rest of the strains, whilst $kpsM^-$, $kpsS^-$ and $kpsC^-$ clustered closely and away from *C.j-WT* and $pglB^-$ along PC1 axis. By contrast, *C.j-WT*, $pglB^-$ and $flaA^-$ strains were separated from the other mutants based on PC2 axis. By visual inspection, the SERS spectra for $flaA^-$ exhibited extra vibrational modes for DNA/
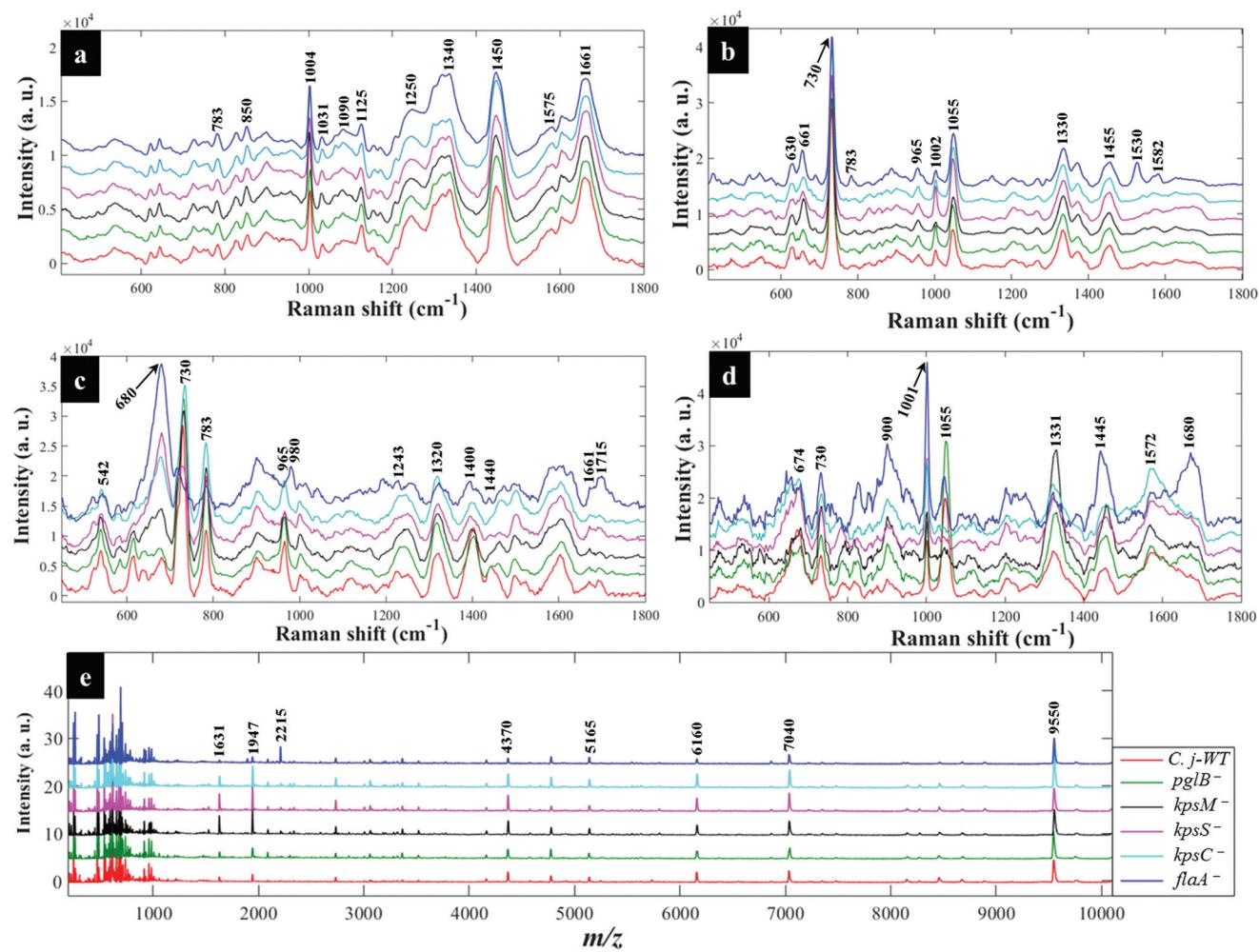
Fig. 3 Typical average spectral data showing characteristic bands measured from *C. jejuni* and mutants examined in this study: (a) Raman spectra (b) *in situ* external SERS (c) SERS by *simple mixing* method (d) *in situ* internal SERS and (e) MALDI-TOF-MS spectra. The colour of each mean spectrum represents individual strains. Spectra are stacked for clarity. Numbers above spectral peaks represent wavenumbers for the major vibrations associated with differentiation of bacteria.

RNA nucleobases at 783 cm^{-1}, proteins at 1149 and 1582 cm^{-1} (C–N stretching), lipid modes at 1530 cm^{-1} (C–H bending and C=C stretching) and combination modes in the deep fingerprint region (420–700 cm^{-1}) which are dominated by carbohydrates and nucleic acids.[48,49] The PCA (Fig. 4b) were consistent with HCA grouping patterns on Fig. 5b.

As in Raman data analysis (Fig. 6a), *kps* mutants were analysed separately by PCA scores (Fig. 6b); where PC1 plane, again, separated *kpsM$^-$* from *kpsS$^-$* and *kpsC$^-$* mutants whilst PC2 discriminated between *kpsS$^-$* and *kpsC$^-$*. The PC1 loadings (Fig. S3a†) particularly for the three mutants highlighted more intense SERS bands for *kpsS$^-$* and *kpsC$^-$* at 730 cm^{-1} (adenine moiety in flavin adenine dinucleotide (FAD),[23,50] and glycosidic ring breathing in *N*-acetylmuramic acid (NAM) and *N*-acetyl-D-glucosamine (NAG) located in the cell wall),[51] 1002 cm^{-1} (ring breathing in phenylalanine) and 1049 cm^{-1} (PO$_2^-$ stretching in FAD, phosphodiester and adenosine triphosphate (ATP)),[48,52] whilst the *kpsM$^-$* mutant produced a more intense band at 661 cm^{-1} (COO$^-$ and C–C bending

modes in carbohydrates/proteins) and lowest level of phenylalanine as suggested by a weak band at 999 cm^{-1} (Fig. 3b).[53–55] Additionally, PC2 loadings (Fig. S3b†) detected the bands at 661 and 730 cm^{-1} which were rather more intense for *kpsS$^-$* than *kpsC$^-$*, as significant variables associated with separation trends on PC2. These band intensity differences especially for carbohydrates and proteins for *in situ* external SERS spectra are consistent with Raman spectra discussed above.

Assessment of PC1 and PC2 loadings for all *in situ* external SERS data showed interesting trends. PC1 loadings (Fig. S4a†) revealed intensity differences for the bands at 661 cm^{-1} (carbohydrates/proteins), 783 cm^{-1} (DNA/RNA bases), and 860 cm^{-1} (C–O–C ring modes in ribose sugars) exhibited greater intensities in *kpsM$^-$* and *flaA$^-$* than the remaining strains. However, *kpsS$^-$* displayed more intense signals at 999 cm^{-1} (phenylalanine) and 1055 cm^{-1} (PO$_2^-$ stretching in ATP, FAD).[56] PC2 loadings (Fig. S4b†) also indicated that *kpsM$^-$* and *flaA$^-$* had relatively intense vibrations at 661 cm^{-1} (carbohydrates/proteins) and a blueshift (shift to higher frequency) at
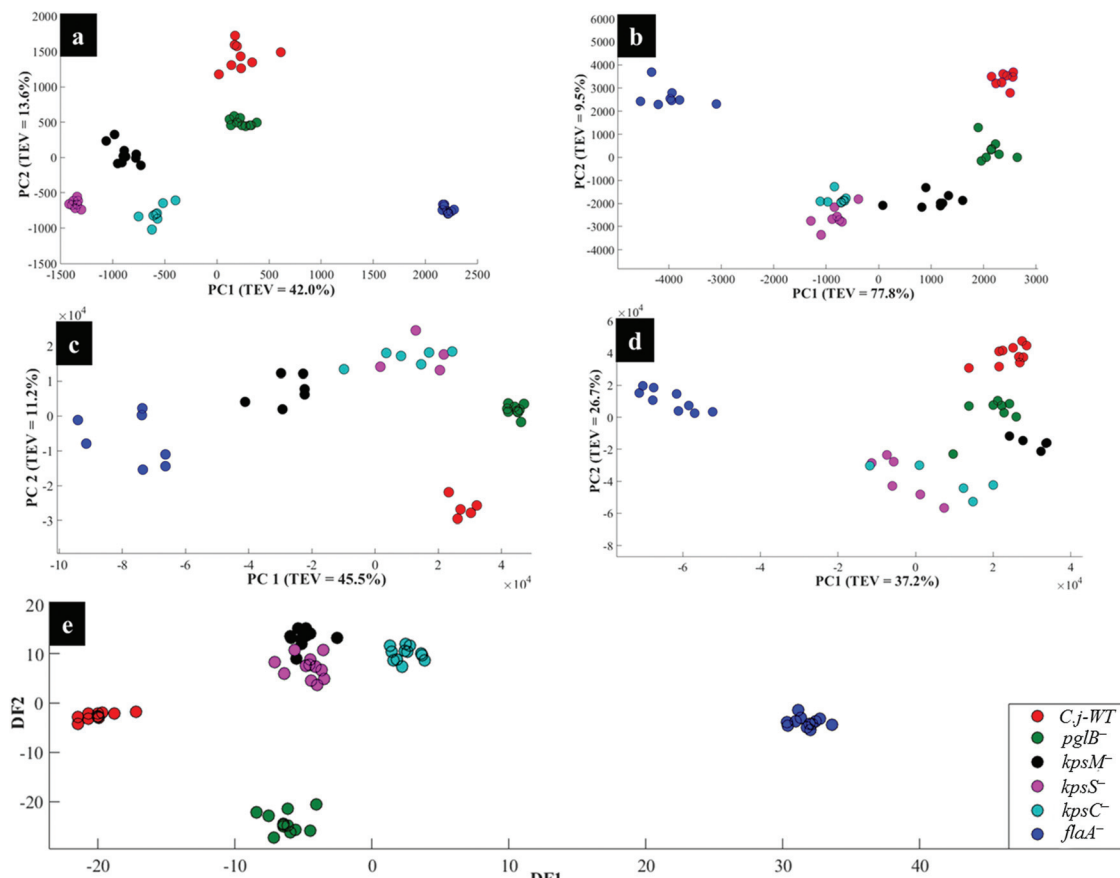
Fig. 4 PCA (a, b, c and d) and DFA (e) scores of spectral data generated by: (a) Raman spectroscopy, (b) *in situ* external SERS, (c) SERS by *simple mixing* method (d), *in situ* internal SERS, and (e) MALDI-TOF-MS of investigated bacteria. Coloured circular symbols represent individual strains, and their designations are provided within the figure.
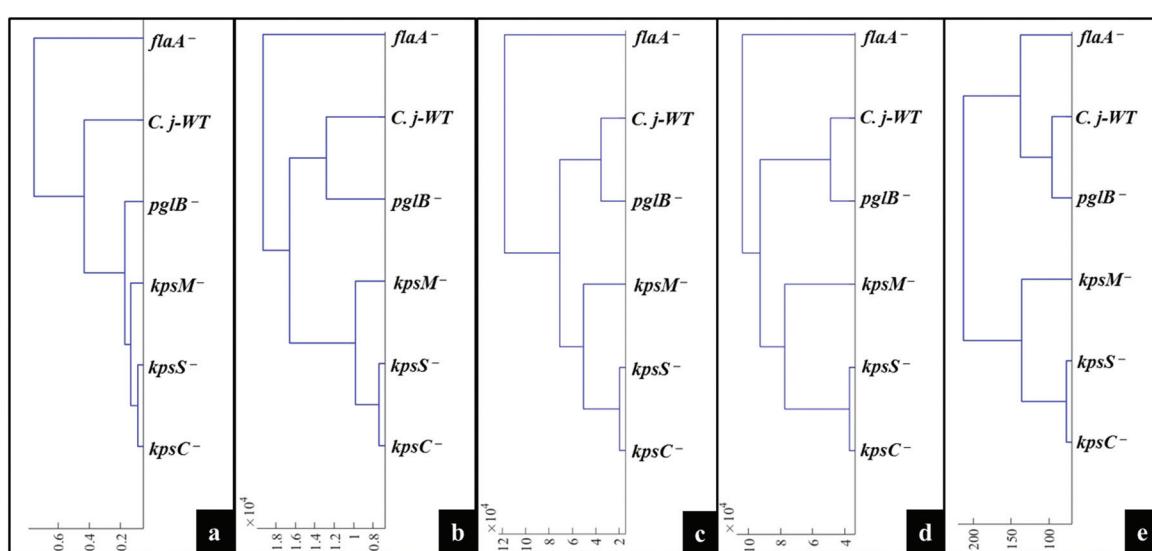

Fig. 5 Representative dendrograms generated by HCA using the averages of PCA (a, b, c and d) and DFA (e) scores of spectral data of bacteria for: (a) Raman spectroscopy, (b) *in situ* external SERS, (c) SERS spectra by *simple mixing* method, (d) *in situ* internal SERS, and (e) MALDI-TOF-MS spectral data.
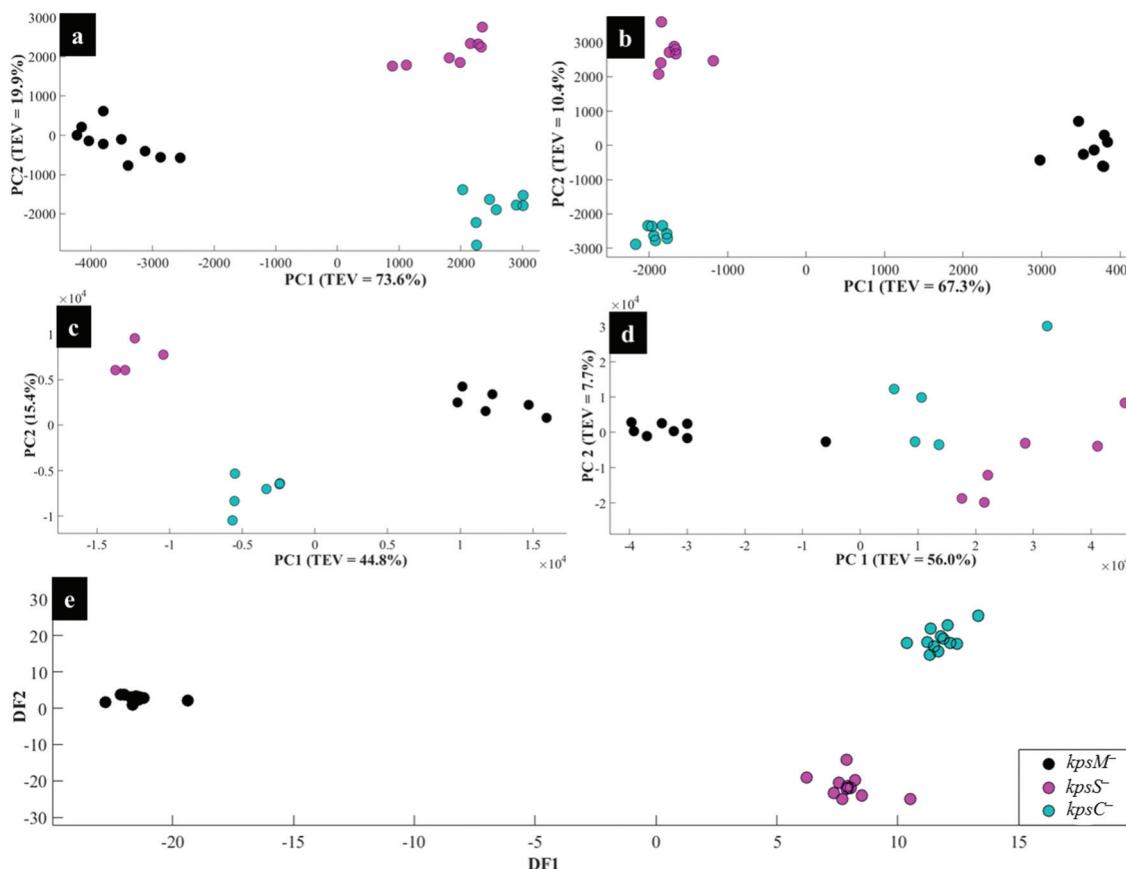
Fig. 6 PCA (a, b, c and d) and DFA (e) scores of spectral data generated using: (a) Raman spectroscopy, (b) *in situ* external SERS, (c) SERS by *simple mixing* method, (d) *in situ* internal SERS, and (e) MALDI-TOF-MS of the *kps* mutants: *kpsM⁻*, *kpsS⁻* and *kpsC⁻*. The coloured symbols represent individual bacterial classes.

730–738 cm⁻¹ (FAD, NAM, NAG). By comparison, intense peaks at 1149, 1530 and 1582 cm⁻¹ on PC2 loadings (Fig. S4b†) were only present on the spectrum of *flaA⁻*, and these peaks are clearly visible on SERS spectra in Fig. 3b.

SERS by *simple mixing* method of bacteria with pre-synthesised AgNPs. The PCA (Fig. 4c) for SERS data involving simple mixing (Fig. 3c) revealed distinctive clustering patterns mediated mainly by cellular constituents on the cell surface (Fig. 2b). The *flaA⁻* strain clustered alone, and away from the remaining samples along PC1. Similarly, *kps* mutants clustered tightly whilst *C.j-WT* and *pglB⁻* mutants were separated along PC1. By contrast, PC2 discriminated *C.j-WT*, *pglB⁻* and *flaA⁻* from *kps* mutants (Fig. 4c). The HCA dendrograms (Fig. 5c) confirmed these relationships, and were also in agreement with *in situ* external SERS data (Fig. 5b).

When the *kps* mutants were analysed separately by PCA (Fig. 6c), *kpsM⁻* separated from *kpsS⁻* and *kpsC⁻* on PC 1, whilst PC2 differentiated *kpsS⁻* from *kpsC⁻*. The clustering trends on PCA were mainly based on 680 cm⁻¹ (guanine ring and C–S stretching) that was stronger in *kpsS⁻* and *kpsC⁻* than *kpsM⁻* mutant whilst the 730 cm⁻¹ band (FAD, NAM, NAG) was less intense in *kpsS⁻* than the other *kps* bacteria as shown by PC1 loadings (Fig. S5a†). Moreover, a blueshift at

965–980 cm⁻¹ (C–N stretching in proteins),[56] was detected. PC2 included strong modes at 783 cm⁻¹ (DNA/RNA), 1400 cm⁻¹ (COO⁻ stretching in proteins), 1440 cm⁻¹ (CH₂ deformation in lipids), and a redshift at 730–738 cm⁻¹ as the differential variants for the PCA clusters (Fig. 6c).

Based on PC1 loadings (Fig. S6a†) for all spectral data measured *via simple mixing*, *flaA⁻*, *kpsS⁻* and *kpsC⁻* cells registered an appreciable band at 680 cm⁻¹, whilst *flaA⁻* also exhibited a unique band at 1715 cm⁻¹ (C=O in esters).[55] Unlike *flaA⁻* mutant, the remaining five strains exhibited an intense discriminatory peak related to adenine vibrations at 730 cm⁻¹. Other significant bands shown by PC1 and PC2 loadings (Fig. S6†) were 783 cm⁻¹ (ring breathing in nucleobases), 1243 cm⁻¹ (C–N stretching, N–H bending in amide III), 1320 cm⁻¹ (ring modes in adenine), 1400 (COO⁻ in proteins) and 1661 cm⁻¹ (C=O, C–N stretching, and N–H bending in amide I), a spectral blueshift at 965–980 cm⁻¹ (C–N stretching in proteins) as well as redshift at 730–738 cm⁻¹ (adenine ring modes).[48,57]

***In situ* production where nanoparticles are located internally in the bacteria.** Interestingly, PCA scores for the *in situ* internal protocol (Fig. 4d) displayed the same clustering patterns as SERS methods discussed above (*in situ* external production

and *simple mixing*), in spite of detecting different discriminatory peaks: external bacterial components compared with internal molecules. PC1 separated all the strains (Fig. 4), with *flaA*⁻ strain forming a single member cluster distinct from *C.j-WT* and the other derived mutants. PC2 isolated three *kps* mutants from other strains. All these clusters of investigated *C. jejuni* cells were grouped accordingly by HCA dendrograms shown in Fig. 5d.

Separate PCA (Fig. 6d) for *in situ* internal SERS data of *kps* mutants were also generated to assess any unique differential bands present for intracellular molecules (Fig. 2c). It was discovered that PC1 loadings (Fig. S7a†) were dominated by strong vibrations at 674 cm⁻¹ (amino acids) and 1001 cm⁻¹ (phenylalanine) bands, which were stronger for *kpsS*⁻ and *kpsC*⁻ compared to *kpsM*⁻ cells. Conversely, the band at 1331 cm⁻¹ (adenine modes) was apparently much stronger for *kpsM*⁻. Other explanatory variants detected at 730 cm⁻¹ (FAD, NAM and NAG), 1445 cm⁻¹ (CH₂ in lipids),[23,24] were demonstrated in PC2 loadings (Fig. S7b†). The internal spectrum of *flaA*⁻ mutant displayed a unique band at 1680 cm⁻¹ (C=O, C–N stretching and N–H bending in proteins), which was clearly absent from all other strains.

For all the *in situ* internal SERS data combined, the PC1 loadings (Fig. S8a†) identified the salient peak at 998 (phenylalanine) that was most intense in *flaA*⁻ compared to the rest of the strains, whereas the band at 1055 cm⁻¹ (PO₂²⁻ in ATP, phosphodiester and FAD) was apparently not detected in *kps* mutants. Besides the bands revealed by PC1 loadings, peaks at 734 and 1331 cm⁻¹ (FAD, NAG, NAM) with varying intensities were detected, with the highest peaks being recorded for *kpsM*⁻ according to PC2 loadings on Fig. S8b.†

MALDI-TOF-MS analysis. In addition, a different physicochemical method was used which targets the proteins found within bacteria. As shown in Fig. 4e, DFA scores of MALDI-TOF-MS data revealed clear differentiation of *C. jejuni* NCTC 11168H and the five derived isogenic mutants. Consistent with Raman and SERS spectra, DFA scores displayed clear separation of the *flaA*⁻ strain from the remaining bacteria according to DF1. By contrast, DF2 revealed the separation of *kps* mutants from the parental wild type strain and other mutants, which again is in complete agreement with vibrational spectroscopy. Similar to the Raman and SERS data, the HCA dendrograms for the mean DFA scores generated from MALDI-TOF-MS data (Fig. 5e) clustered the *kps* samples together and separately from the wild type and other mutants. However, as opposed to vibrational spectral data, MALDI-TOF-MS data classified *C.j-WT*, *pglB*⁻ and *flaA*⁻ within the same clade but on completely different branches (Fig. 5e).

The DFA scores generated from MALDI-TOF-MS data for *kps* cells (Fig. 6e) separated *kpsM*⁻ from *kpsS*⁻ and *kpsC*⁻ along DF1, and between *kpsS*⁻ and *kpsC*⁻ along DF2. DF1 loadings (Fig. S9†) for *kps* mutants only indicated more intense peaks at 1631, 1947 and 7040 *m/z* ratios[32] for *kpsS*⁻ and *kpsC*⁻. Conversely, the molecular ions at 4778 and 9550 *m/z* were more intense in *kpsM*⁻. DF2 loadings (Fig. S9a†) showed stronger bands at *m/z* 2734, 4370 and 6160 for the *kpsS*⁻ and *kpsC*⁻ relative to *kpsM*⁻.

The DFA loadings for MALDI-TOF-MS data of all bacterial cells (Fig. S10†) identified ions of varying intensities in the *m/z* 1631–9550 range. The peaks for molecular ions with *m/z* 4370 and 6160 were very weak in the *flaA*⁻ mutant but strongly intense in the rest of the strains. By contrast, the band with *m/z* 2215 was very intense in *flaA*⁻ mutant but extremely weak in the other five strains. However, biomarker bands detected at *m/z* 5165, 7040 and 9550, which are tentatively linked to various bacterial ribosomal and membrane proteins,[58] displayed similar intensities in *C. jejuni* and mutants.

Discussions

The aim of this study was to characterise bacterial mutants of a single *C. jejuni* strain that express different phenotypes. The five mutants exhibited molecular changes in extracellular biocomponents (*viz.* polysaccharides and proteins) on the cell wall surface as a consequence of gene mutations as described in Fig. 2. Thus, three rapid fingerprinting tools (Raman, SERS and MALDI-TOF-MS) aimed to access this intracellular and extracellular biochemical information in *C. jejuni* strains. In particular, the *simple mixing* and *in situ* external SERS methods were designed to provide structural and abundance dynamics of molecules present on the cell wall (*e.g.* FAD, LPS, *etc.*), whilst *in situ* internal SERS revealed complementary spectral information from molecules located in the cytoplasm (*e.g.* amino acids, DNA/RNA) of cells. In addition, since gene mutations resulted in changes in the abundance, identity and structure of specific cell surface proteins; MALDI-TOF-MS was specially applied to give deeper insights into changes in proteins in the examined mutants. The SERS trilogy (*simple mixing* and two *in situ* methods) and MALDI-TOF-MS tools were further complemented by Raman spectroscopy, which provides whole-organism biochemical fingerprint. However, the spectra obtained from the applied techniques are multidimensional by nature, and so the discrimination of bacteria by visual screening only was difficult. This emphasised the need to apply unsupervised (PCA) and supervised (DFA) analyses for dimensionality reduction to guide differentiation of bacteria. Despite exhibiting different selection rules for biochemical detection,[59,60] spectral data acquired from Raman, SERS and MALDI-TOF-MS differentiated between the parental strain and derived mutants examined in this study. The PCA and DFA scores generated from respective spectral data consistently separated *flaA*⁻ from the remaining mutants (Fig. 4). The HCA dendrograms constructed from the averages of PCA and DFA scores also confirmed separate groupings; where *flaA*⁻ formed a single isolated group, whilst the *kps* mutants consistently formed a separate three-member grouping which clustered away from *C.j-WT* and *pglB*⁻. Raman differentiated *C.j-WT* from *pglB*⁻ (Fig. 5a) as opposed to SERS and MALDI-TOF-MS, which classified these two strains in the same group. Although *C.j-WT*,

$pglB^-$ and $flaA^-$ were separated based on phenotypic dynamics, MALDI-TOF-MS data assigned these strains under one grouping as shown by HCA dendrograms (Fig. 5e).

As evidenced by dynamics in spectral features, the clustering trends on PCA and DFA scores and HCA grouping patterns were as a result of chemical and structural differences between the wild type strain and five derived isogenic mutants. The $flaA^-$ mutant lacks single bipolar unsheathed helical flagella (Fig. 1) making it non-motile, and clearly different from other strains. The $flaA^-$ mutant lacks the flagellar filament FlaA protein, and so it can assemble a basal body type structure in the inner and outer cell membrane but no long filament type structure is produced. MALDI-TOF-MS spectra and corresponding loadings plots revealed diagnostic peaks at m/z 4370 and 6160 that are very weak in the spectrum of $flaA^-$ mutant but, by far, strongly intense in $C.j\text{-}WT$, $plgB^-$ and kps strains. These molecular ions contributed significantly to the clustering patterns observed on the PCA and DFA (Fig. 4). In contrast, the mutants in kps genes ($kpsC^-$, $kpsM^-$ and $kpsS^-$) that abolish capsule formation consistently clustered closely together. Further investigation of these three mutants by PCA (Raman and SERS) and DFA (MALDI-TOF-MS) scores (Fig. 6) highlighted clear separations among them due to phenotypic variations. That is to say, whilst KpsS and KpsC proteins play vital functions in the biosynthesis and assembly of cytoplasmic CPS before transport, the KpsM protein is a component of the export machinery for transporting CPS across the bacterial inner membrane as depicted in Fig. 1.[11,61] To be more specific, KpsS and KpsC are 3-deoxy-D-manno-oct-2-ulosonic acid (Kdo) transferases that add initial Kdo residues to the phospholipid carrier on the cytoplasmic face of inner membrane prior to addition of CPS and transport to the cell surface.[11,62] Thus, $kpsM^-$ mutant is expected to accumulate cytoplasmic phospholipid-linked CPS which is only blocked in transport but not in biosynthesis.[42] Conversely, $kpsS^-$ and $kpsC^-$ strains would, to a large extent, not accumulate phospholipid-linked CPS since lipid acceptors need priming with Kdo residues, though they may accumulate unlinked CPS in the cytoplasm,[63] as evidenced by the presence of polysaccharide Raman and SERS bands in the fingerprint region (400–900 cm^{-1}). The Raman (Fig. S1†) and *in situ* internal SERS (Fig. S7†) data also revealed diagnostic peaks measured from intracellular polysaccharides and proteins for kps cells that contributed to the separations observed on PCA and DFA (Fig. 4). These bands were predominantly differentiated *via* intensity variations between 400 and 900 cm^{-1}, and at 1050 cm^{-1}; the spectral region linked to polysaccharide vibrations.[45,64] The *simple mixing* and *in situ* external SERS also displayed similar bands in the same frequency range (Fig. S3 and S5†); however, these bands were predominantly derived from cell wall molecules (Fig. 2a and b). On the other hand, *C. j-WT* exhibits natural phenotype as *C. jejuni* is found in nature, which is why it formed a distinctive cluster. By contrast, $pglB^-$ clustered separately by virtue of having non-functional *N*-linked oligosaccharyltransferase enzyme, resulting in numerous cell surface proteins lacking one or more heptasac-

charide *N*-linked glycans (Fig. 1).[65] The mutants investigated in this study were constructed through the insertion of a kanamycin resistance gene, and this may potentially contribute to the discrimination from the *C.j-WT* strain, which does not contain this cassette. Nonetheless, the kanamycin resistance gene was present in all the mutants and thus it should not contribute to differentiation amongst them.

Previous research indicates that several tools such as pyrolysis MS,[66–68] Fourier-transform infrared (FT-IR),[25,69–72] and UV resonance Raman (UVRR)[73–75] are widely used in parallel with multivariate analysis for accurate identification of bacteria. Among spectroscopic tools, Raman and SERS are powerful sampling platforms capable of generating phenotypes from slurry and single cells non-destructively,[41,47,76–78] and *in situ* in aqueous biological systems where pathogens are naturally found.[79–81] By combining molecular sensitivity, selectivity and specificity, Raman and SERS are perhaps ideally suitable for rapid detection of fastidious microbes, including *Campylobacter* spp.[16,25,82] Like Raman spectroscopy, SERS methods applied in the present study are label-free, implying that plasmonic substrates were in direct contact with cellular biomolecules. Hence, SERS spectra represent real bacterial phenotypes determined by underlying biological processes, which differs from indirect SERS based on Raman reporters and recognition elements *e.g.* dyes, antibodies.[83] Despite showing potential for bacterial detection, label-free SERS demands careful optimisation of protocols to ensure clinically desirable robustness and reproducibility,[84,85] and especially so when differentiating closely related pathogens. In this study, we designed SERS approaches in which AgNPs were synthesised *in situ* (in the presence of cells) to improve chemical interactions with molecules, resulting in uniform spectra of negligible fluorescence backgrounds.[24]

SERS involving *in situ* assays employing various reductants and oxidants as precursors have been exploited for bacterial detection,[34,86,87] since pioneering work by Efrima and Zeiri.[23] Recently, Chen and co-workers also reported *in situ* near infrared-SERS probes designed to access cell wall and intracellular biomolecules for clinical isolates.[64] A key limitation of this method was that the SERS spectra for *in situ* internal strategy displayed only two weak spectral bands at 890 and 1040 cm^{-1}.[64] By contrast, three SERS assays reported here using the same precursors for AgNPs synthesis recorded multivariable spectra consisting of intense peaks which proved to be practical for discriminating *C. jejuni* pathogens.

The strains examined in this study exhibited varied molecular composition and chemical bond linkages in biomolecules present in the cytoplasm and cell envelope as a result of mutations.[11] Our SERS assays with NPs localised within extra or intracellular parts of cells were meant, in principle, to capture this characteristic chemical information and associated phenotypes in an untargeted way, given that AgNPs have high affinity for electronegative atoms (N, O, S, *etc.*) naturally present in biomolecules.[88] For example, our SERS protocols proved to be sensitive towards nitrogen and oxygen-rich FAD and adenine-related vibrations detected at 730, 1320 and

1330 cm^{-1} (Fig. 3b and c). FAD is a co-enzyme which regulates enzymatic redox metabolic reactions such as respiration,[89] and *N*- or *O*-linked glycosylation processes related to virulence factors of the pathogens.[65,90] In addition, SERS complemented Raman data by providing insights into molecular dynamics in LPS; the major component of the outer membrane of Gram-negative cells, which mediates adhesion of bacteria to human epithelial cells.[91] Considering that the cell wall is the part of a bacterium which is in direct contact with the human gut during microbial infection, elucidating surface molecular composition and structural dynamics of pathogens by SERS may be crucial for predicting the induction and extent of gastroenteritis, differential diagnostics and choice of therapeutics for infections induced by closely related etiological agents,[92] as demonstrated for methicillin-resistant and sensitive *Staphylococcus aureus*.[93] The SERS assays used in this study generated similar PCA scores and HCA dendrograms, though the spectra were derived from different molecular moieties as evidenced by dynamic and diverse bands. This not only indicated improved reproducibility of these techniques, and robust classification accuracy at strain level, which are comparable to other biosensors.[12,94] Whilst MALDI-TOF-MS is destructive, it has established workflow, rapid library search and identification of protein masses measured from clinical isolates.[95] Importantly, MALDI-TOF-MS offers a snapshot of essential protein biomarkers in the proteome and transcriptome that regulate physiological and metabolic functions of bacteria,[96] with similar accuracy level as conventional techniques such as 16S rRNA sequencing,[25] and Vitek 2™ systems.[97]

Therefore, in clinical diagnostics Raman, SERS and MALDI-TOF-MS optical tools represent an exciting holistic approach with considerable potential for conveying simultaneously, complementary and confirmatory phenotypes for *C. jejuni*,[13] and how such cellular properties may affect the interactions with the human gut. It is also worth noting that all analytical tools applied in this study showed distinctive advantages over traditional and molecular methods. Firstly, they are rapid (spectral acquisition time: 15 s, 2 s and 3 min for Raman, SERS and MALDI-TOF-MS, respectively), making them ideal for high-throughput screening of many infectious pathogens be it at genus, species or subspecies level. Secondly, they employ simple sample preparation methods, and obtain information-rich biochemical information from small sample volumes, as low as 1 pL (Raman and SERS). Since Raman and SERS may preserve cell integrity, bacteria can potentially be re-cultivated and used for further downstream studies such as genomics, lipidomics and metabolomics.[25,98]

Conclusions

We have demonstrated the applicability of Raman spectroscopy, SERS and MALDI-TOF-MS for intra-strain level discrimination of mutants of the bacterium *C. jejuni* analysis. SERS involving *in situ* external and internal deposition of AgNPs were successfully used to probe extra- and intracellular polysaccharides and proteins present in the parental *C. jejuni* strain and its mutants. Interestingly, all analytical techniques applied in this study clearly differentiated among near isogenic mutants of the foodborne pathogen *C. jejuni*. Multivariate analysis of spectra *via* PCA (Raman and SERS) and DFA (MALDI-TOF-MS) scores revealed distinctive clusters indicating phenotypic dynamics for individual mutants, which were confirmed by HCA dendrograms. In addition, using Raman, SERS and MALDI-TOF-MS, we discriminated between three *kps* mutants which express similar phenotypes. The major MALDI-TOF-MS biomarkers that are, perhaps, related to flagellin protein (FlaA) fragments were detected at *m*/*z* 4370 and 6160. These peaks were very weak in *flaA*⁻ mutant compared to *C.j-WT*, *plgB*⁻ and *kps* strains. Other molecular ions detected on MALDI-TOF-MS spectra had similar intensities for all the strains examined in this study, suggesting that capsular polysaccharides did not contribute significantly to the differentiation of mutants. Nevertheless, various polysaccharides signals were detected by SERS measured *via in situ* approaches, and these were important variables in the characterisation of mutants. Based on the biochemical variations of near isogenic mutants and subsequent spectral findings, Raman and SERS exhibited greater specificity and rapidity. Collectively, our fingerprinting platforms represent powerful integrated techniques which may be suitable for rapid and accurate mutant verification and testing of clinically relevant pathogens for spontaneous loss of flagella or capsule within clinical and epidemiological food poisoning research.

Conflicts of interest

The authors have no conflicts of interest to declare.

Acknowledgements

References

1 World Health Organisation, Available online: https://www.who.int/en/news-room/fact-sheets/detail/campylobacter (accessed on 13 August, 2019).

2 D. I. Ellis, H. Muhamadali, M. Chisanga and R. Goodacre, *Encycl. Food Chem.*, 2019, **1**, 364–370.

3 D. Y. He, Z. Z. Wu, B. Cui, E. B. Xu and Z. Y. Jin, *Food Chem.*, 2019, **289**, 708–713.

4   European Food Safety and European Centre for Disease Prevention and Control, *EFSA J.*, 2018, **16**, 5500–5761.

5   European Food Safety and European Centre for Disease Prevention and Control, *EFSA J.*, 2016, **14**, 4634–1664.

6   European Food Safety and European Centre for Disease Prevention and Control, *EFSA J.*, 2015, **13**, 4329–4518.

7   E. Frirdich, J. Biboy, M. Pryjma, J. Lee, S. Huynh, C. T. Parker, S. E. Girardin, W. Vollmer and E. C. Gaynor, *Mol. Microbiol.*, 2019, **112**, 280–301.

8   J. Parkhill, B. W. Wren, K. Mungall, J. M. Ketley, C. Churcher, D. Basham, T. Chillingworth, R. M. Davies, T. Feltwell, S. Holroyd, K. Jagels, A. V. Karlyshev, S. Moule, M. J. Pallen, C. W. Penn, M. A. Quail, M. A. Rajandream, K. M. Rutherford, A. H. M. van Vliet, S. Whitehead and B. G. Barrell, *Nature*, 2000, **403**, 665–668.

9   J. Tian, C. F. Cao, T. Li, K. Zhang, P. F. Li, Y. L. Liu and X. Y. Liu, *Front. Neurol.*, 2019, **10**, 714–720.

10   O. Sahin, S. A. Terhorst, E. R. Burrough, Z. Q. Shen, Z. W. Wu, L. Dai, Y. Z. Tang, P. J. Plummer, J. Ji, M. J. Yaeger and Q. J. Zhang, *Infect. Immun.*, 2017, **85**, 1–15.

11   L. M. Willis and C. Whitfield, *Proc. Natl. Acad. Sci. U. S. A.*, 2013, **110**, 20753–20758.

12   O. Lazcka, F. J. Del Campo and F. X. Munoz, *Biosens. Bioelectron.*, 2007, **22**, 1205–1217.

13   Y. H. Liu, W. Yamazaki, Y. T. Huang, C. H. Liao, W. H. Sheng and P. R. Hsueh, *J. Microbiol., Immunol. Infect.*, 2019, **52**, 122–131.

14   D. Martiny, A. Dediste, L. Debruyne, L. Vlaes, N. B. Haddou, P. Vandamme and O. Vandenberg, *Clin. Microbiol. Infect.*, 2011, **17**, 1001–1006.

15   D. Q. Zhong and W. Q. He, *J. Nanosci. Nanotechnol.*, 2019, **19**, 5517–5521.

16   M. Chisanga, H. Muhamadali, D. I. Ellis and R. Goodacre, *Appl. Spectrosc.*, 2018, **72**, 987–1000.

17   O. Samek, H. H. Telle, L. G. Harris, M. Bloomfield and D. Mack, *Laser Phys. Lett.*, 2008, **5**, 465–470.

18   M. J. Tang, G. D. McEwen, Y. Z. Wu, C. D. Miller and A. H. Zhou, *Anal. Bioanal. Chem.*, 2013, **405**, 1577–1591.

19   J. B. Xu, L. Preciado-Llanes, A. Aulicino, C. M. Decker, M. Depke, M. G. Salazar, F. Schmidt, A. Simmons and W. E. Huang, *Anal. Chem.*, 2019, **91**, 7729–7737.

20   K. S. Lee, M. Palatinszky, F. C. Pereira, J. Nguyen, V. I. Fernandez, A. J. Mueller, F. Menolascina, H. Daims, D. Berry, M. Wagner and R. Stocker, *Nat. Microbiol.*, 2019, **4**, 1035–1048.

21   W. E. Huang, M. Q. Li, R. M. Jarvis, R. Goodacre and S. A. Banwart, in *Advances in Applied Microbiology*, ed. A. I. Laskin, S. Sariaslani and G. M. Gadd, Elsevier Academic Press Inc, San Diego, 2010, vol. 70, pp. 153–186.

22   S. Schlucker, *Angew. Chem., Int. Ed.*, 2014, **53**, 4756–4795.

23   S. Efrima and L. Zeiri, *J. Raman Spectrosc.*, 2009, **40**, 277–288.

24   L. Zeiri, B. V. Bronk, Y. Shabtai, J. Eichler and S. Efrima, *Appl. Spectrosc.*, 2004, **58**, 33–40.

25   H. Muhamadali, D. Weaver, A. Subaihi, N. AlMasoud, D. K. Trivedi, D. I. Ellis, D. Linton and R. Goodacre, *Analyst*, 2016, **141**, 111–122.

26   R. E. Mandrell, L. A. Harden, A. Bates, W. G. Miller, W. F. Haddon and C. K. Fagerquist, *Appl. Environ. Microbiol.*, 2005, **71**, 6292–6307.

27   M. Alispahic, K. Hummel, D. Jandreski-Cvetkovic, K. Nobauer, E. Razzazi-Fazeli, M. Hess and C. Hess, *J. Med. Microbiol.*, 2010, **59**, 295–301.

28   N. AlMasoud, Y. Xu, D. K. Trivedi, S. Salivo, T. Abban, N. J. W. Rattray, E. Szula, H. AlRabiah, A. Sayqal and R. Goodacre, *Anal. Bioanal. Chem.*, 2016, **408**, 7865–7878.

29   T. Krishnamurthy, P. L. Ross and U. Rajamani, *Rapid Commun. Mass Spectrom.*, 1996, **10**, 883–888.

30   N. AlMasoud, Y. Xu, D. I. Ellis, P. Rooney, J. F. Turton and R. Goodacre, *Anal. Methods*, 2016, **8**, 7603–7613.

31   S. Savas, G. Hazirolan, A. Karagoz and M. Parlak, *J. Microbiol. Methods*, 2019, **162**, 62–68.

32   P. Lasch, D. Jacob, R. Grunow, T. Schwecke and J. Doellinger, *TrAC, Trends Anal. Chem.*, 2016, **85**, 103–111.

33   N. AlMasoud, Y. Xu, N. Nicolaou and R. Goodacre, *Anal. Chim. Acta*, 2014, **840**, 49–57.

34   M. Chisanga, H. Muhamadali, R. Kimber and R. Goodacre, *Faraday Discuss.*, 2017, **205**, 331–343.

35   J. A. Creighton, C. G. Blatchford and M. G. Albrecht, *J. Chem. Soc., Faraday Trans. 2*, 1979, **75**, 790–798.

36   H. Muhamadali, M. Chisanga, A. Subaihi and R. Goodacre, *Anal. Chem.*, 2015, **87**, 4578–4586.

37   P. H. C. Eilers, *Anal. Chem.*, 2004, **76**, 404–411.

38   H. Martens, J. P. Nielsen and S. B. Engelsen, *Anal. Chem.*, 2003, **75**, 394–404.

39   P. Geladi, B. Sethson, J. Nystrom, T. Lillhonga, T. Lestander and J. Burger, *Spectrochim. Acta, Part B*, 2004, **59**, 1347–1357.

40   H. J. H. Macfie, C. S. Gutteridge and J. R. Norris, *J. Gen. Microbiol.*, 1978, **104**, 67–74.

41   Z. Q. Lin, X. Zhao, J. Q. Huang, W. Liu, Y. T. Zheng, X. Yang, Y. Zhang, M. L. de la Chapelle and W. L. Fu, *Analyst*, 2019, **144**, 2803–2810.

42   A. V. Karlyshev, D. Linton, N. A. Gregson, A. J. Lastovica and B. W. Wren, *Mol. Microbiol.*, 2000, **35**, 529–541.

43   M. E. Konkel, J. D. Klena, V. Rivera-Amill, M. R. Monteville, D. Biswas, B. Raphael and J. Mickelson, *J. Bacteriol.*, 2004, **186**, 3296–3303.

44   I. A. Hajam, P. A. Dar, I. Shahnawaz, J. C. Jaume and J. H. Lee, *Exp. Mol. Med.*, 2017, **49**, 373–387.

45   K. Maquelin, C. Kirschner, L. P. Choo-Smith, N. van den Braak, H. P. Endtz, D. Naumann and G. J. Puppels, *J. Microbiol. Methods*, 2002, **51**, 255–271.

46   J. De Gelder, K. De Gussem, P. Vandenabeele and L. Moens, *J. Raman Spectrosc.*, 2007, **38**, 1133–1147.

47   S. Jaafreh, O. Valler, J. Kreyenschmidt, K. Gunther and P. Kaul, *Talanta*, 2019, **202**, 411–425.

48   A. Walter, A. Marz, W. Schumacher, P. Rosch and J. Popp, *Lab Chip*, 2011, **11**, 1013–1021.

49   M. Kahraman, M. M. Yazici, F. Sahin, O. F. Bayrak and M. Culha, *Appl. Spectrosc.*, 2007, **61**, 479–485.

50 P. Kubryk, R. Niessner and N. P. Ivleva, *Analyst*, 2016, **141**, 2874–2878.

51 R. M. Jarvis and R. Goodacre, *Anal. Chem.*, 2004, **76**, 40–47.

52 W. R. Premasiri, J. C. Lee, A. Sauer-Budge, R. Theberge, C. E. Costello and L. D. Ziegler, *Anal. Bioanal. Chem.*, 2016, **408**, 4631–4647.

53 M. Graff and J. Bukowska, *Vib. Spectrosc.*, 2010, **52**, 103–107.

54 K. Kneipp, A. S. Haka, H. Kneipp, K. Badizadegan, N. Yoshizawa, C. Boone, K. E. Shafer-Peltier, J. T. Motz, R. R. Dasari and M. S. Feld, *Appl. Spectrosc.*, 2002, **56**, 150–154.

55 Y. F. Xie, L. Xu, Y. Q. Wang, J. D. Shao, L. Wang, H. Y. Wang, H. Qian and W. R. Yao, *Anal. Methods*, 2013, **5**, 946–952.

56 M. Culha, A. Adiguzel, M. M. Yazici, M. Kahraman, F. Sahin and M. Gulluce, *Appl. Spectrosc.*, 2008, **62**, 1226–1232.

57 A. Sengupta, M. Mujacic and E. J. Davis, *Anal. Bioanal. Chem.*, 2006, **386**, 1379–1386.

58 D. Ziegler, J. F. Pothier, J. Ardley, R. K. Fossou, V. Pfluger, S. de Meyer, G. Vogel, M. Tonolla, J. Howieson, W. Reeve and X. Perret, *Appl. Microbiol. Biotechnol.*, 2015, **99**, 5547–5562.

59 E. Smith and G. Dent, *Modern Raman Spectroscopy: A Practical Approach*, Blackwell Science Publ, Oxford, 2005.

60 K. S. Jang and Y. H. Kim, *J. Microbiol.*, 2018, **56**, 209–216.

61 L. M. Willis and C. Whitfield, *Carbohydr. Res.*, 2013, **378**, 35–44.

62 C. R. H. Raetz and C. Whitfield, *Annu. Rev. Biochem.*, 2002, **71**, 635–700.

63 G. P. Rigg, B. Barrett and I. S. Roberts, *Microbiology*, 1998, **144**, 2905–2914.

64 L. Y. Chen, N. Mungroo, L. Daikuara and S. Neethirajan, *J. Nanobiotechnol.*, 2015, **13**, 45–53.

65 J. Kelly, H. Jarrell, L. Millar, L. Tessier, L. M. Fiori, P. C. Lau, B. Allan and C. M. Szymanski, *J. Bacteriol.*, 2006, **188**, 2427–2434.

66 D. Melucci, S. Fedi, M. Locatelli, C. Locatelli, S. Montalbani and M. Cappelletti, *Curr. Drug Targets*, 2013, **14**, 1023–1033.

67 R. Goodacre, E. M. Timmins, R. Burton, N. Kaderbhai, A. M. Woodward, D. B. Kell and P. J. Rooney, *Microbiology*, 1998, **144**, 1157–1170.

68 X. Li, P. T. Lv, L. Wang, A. L. Guo, M. H. Ma and X. B. Qi, *J. Chromatogr. B: Anal. Technol. Biomed. Life Sci.*, 2014, **971**, 107–111.

69 D. J. M. Mouwen, M. Weijtens, R. Capita, C. Alonso-Calleja and M. Prieto, *Appl. Environ. Microbiol.*, 2005, **71**, 4318–4324.

70 D. J. M. Mouwen, R. Capita, C. Alonso-Calleja, J. Prieto-Gomez and M. Prieto, *J. Microbiol. Methods*, 2006, **67**, 131–140.

71 Z. Cao, Z. J. Wang, Z. L. Shang and J. C. Zhao, *PLoS One*, 2017, **12**, 172359–172373.

72 L. Mariey, J. P. Signolle, C. Amiel and J. Travert, *Vib. Spectrosc.*, 2001, **26**, 151–159.

73 E. C. Lopez-Diez and R. Goodacre, *Anal. Chem.*, 2004, **76**, 585–591.

74 R. M. Jarvis and R. Goodacre, *FEMS Microbiol. Lett.*, 2004, **232**, 127–132.

75 K. Gaus, P. Rosch, R. Petry, K. D. Peschke, O. Ronneberger, H. Burkhardt, K. Baumann and J. Popp, *Biopolymers*, 2006, **82**, 286–290.

76 L. Z. Guo, C. S. Ye, L. Cui, K. Wan, S. Chen, S. H. Zhang and X. Yu, *Environ. Int.*, 2019, **130**, 104883–104893.

77 W. E. Huang, R. I. Griffiths, I. P. Thompson, M. J. Bailey and A. S. Whiteley, *Anal. Chem.*, 2004, **76**, 4452–4458.

78 R. Weiss, M. Palatinszky, M. Wagner, R. Niessner, M. Elsner, M. Seidel and N. P. Ivleva, *Analyst*, 2019, **144**, 943–953.

79 B. Lorenz, C. Wichmann, S. Stockel, P. Rosch and J. Popp, *Trends Microbiol.*, 2017, **25**, 413–424.

80 M. K. Song, L. F. Jiang, D. Y. Zhang, C. L. Luo, H. Yin, Y. T. Li and G. Zhang, *J. Hazard. Mater.*, 2018, **353**, 534–541.

81 Y. Z. Song, A. K. Kaster, J. Vollmers, Y. Q. Song, P. A. Davison, M. Frentrup, G. M. Preston, I. P. Thompson, J. C. Murrell, H. B. Yin, C. N. Hunter and W. E. Huang, *Microb. Biotechnol.*, 2017, **10**, 125–137.

82 X. N. Lu, Q. Huang, W. G. Miller, D. E. Aston, J. Xu, F. Xue, H. W. Zhang, B. A. Rasco, S. Wang and M. E. Konkel, *J. Clin. Microbiol.*, 2012, **50**, 2932–2946.

83 H. Kearns, R. Goodacre, L. E. Jamieson, D. Graham and K. Faulds, *Anal. Chem.*, 2017, **89**, 12666–12673.

84 M. Kahraman, M. M. Yazici, F. Sahin and M. Culha, *J. Biomed. Opt.*, 2007, **12**, 540151–540156.

85 H. Fisk, C. Westley, N. J. Turner and R. Goodacre, *J. Raman Spectrosc.*, 2016, **47**, 59–66.

86 H. B. Zhou, D. T. Yang, N. P. Ivleva, N. E. Mircescu, S. Schubert, R. Niessner, A. Wieser and C. Haisch, *Anal. Chem.*, 2015, **87**, 6553–6561.

87 H. B. Zhou, D. T. Yang, N. P. Ivleva, N. E. Mircescu, R. Niessner and C. Haisch, *Anal. Chem.*, 2014, **86**, 1525–1533.

88 M. Chisanga, H. Muhamadali, D. I. Ellis and R. Goodacre, *Appl. Sci.*, 2019, **9**, 1163–1186.

89 S. O. Mansoorabadi, C. J. Thibodeaux and H. W. Liu, *J. Org. Chem.*, 2007, **72**, 6329–6342.

90 C. Schaffer and P. Messner, *FEMS Microbiol. Rev.*, 2017, **41**, 49–91.

91 G. Zhang, T. C. Meredith and D. Kahne, *Curr. Opin. Microbiol.*, 2013, **16**, 779–785.

92 A. M. Teixeira, A. Nemec and C. Sousa, *Molecules*, 2019, **24**, 168–177.

93 L. I. Llarrull, J. F. Fisher and S. Mobashery, *Antimicrob. Agents Chemother.*, 2009, **53**, 4051–4063.

94 V. Velusamy, K. Arshak, O. Korostynska, K. Oliwa and C. Adley, *Biotechnol. Adv.*, 2010, **28**, 232–254.

95 E. Nagy, S. Becker, M. Kostrzewa, N. Barta and E. Urban, *J. Med. Microbiol.*, 2012, **61**, 1393–1400.

96 A. Mellmann, J. Cloud, T. Maier, U. Keckevoet, I. Ramminger, P. Iwen, J. Dunn, G. Hall, D. Wilson,

P. LaSala, M. Kostrzewa and D. Harmsen, *J. Clin. Microbiol.*, 2008, **46**, 1946–1954.

97 A. Kassim, V. Pfluger, Z. Premji, C. Daubenberger and G. Revathi, *BMC Microbiol.*, 2017, **17**, 128–135.

98 M. R. Mashego, K. Rumbold, M. De Mey, E. Vandamme, W. Soetaert and J. J. Heijnen, *Biotechnol. Lett.*, 2007, **29**, 1–16.

99 A. V. Karlyshev, D. Linton, N. A. Gregson and B. W. Wren, *Microbiology*, 2002, **148**, 473–480.